Metasurface-Assisted Quantum Nonlocal Weak-Measurement Microscopy

Jiawei Liu,[1] Qiang Yang,[1] Yichang Shou,[1] Shizhen Chen,[1] Weixing Shu,[1] Geng Chen,[2] Shuangchun Wen,[1] and Hailu Luo[1,*]

[1]Laboratory for Spin Photonics, School of Physics and Electronics, Hunan University, Changsha 410082, China
[2]CAS Key Laboratory of Quantum Information, University of Science and Technology of China, Hefei 230026, China

(Received 7 April 2023; accepted 2 January 2024; published 25 January 2024)

In standard quantum weak measurements, preselection and postselection of quantum states are implemented in the same photon. Here we go beyond this restrictive setting and demonstrate that the preselection and postselection can be performed in two different photons, if the two photons are polarization entangled. The Pancharatnam-Berry phase metasurface is incorporated in the weak measurement system to perform weak coupling between probe wave function and spin observable. By introducing nonlocal weak measurement into the microscopy imaging system, it allows us to remotely switch different microscopy imaging modes of pure-phase objects, including bright-field, differential, and phase reconstruction. Furthermore, we demonstrate that the nonlocal weak-measurement scheme can prevent almost all environmental noise photons from detection and thus achieves a higher image contrast than the standard scheme at a low photon level. Our results provide the possibility to develop a quantum nonlocal weak-measurement microscope for label-free imaging of transparent biological samples.

DOI: 10.1103/PhysRevLett.132.043601

Quantum weak measurement, as an important extension of quantum measurement, was first introduced by Aharonov, Albert, and Vaidman [1]. In quantum mechanics, measurement can be regarded as the coupling of an observable and a probe state that leads to the transition of a pointer [2]. The result of a measurement can be read out from a pointer shift δ_i. In general, the conventional quantum measurement is involved in strong coupling and the probe wave function is distorted. If the probe state is a Gaussian distribution with width w, the strong coupling occurs in the regime of $\delta_i \gg w$. The average measurement result must be bounded between the smallest and largest of its eigenvalues. Weak measurement occurs in the opposite regime, where the pointer shift is much less than the width of the probe state, $\delta_i \ll w$ [3]. In this case, so little information is extracted that the probe state does not collapse. The weak value is the average of measurement results which can lay outside of the eigenvalues of the observable [4,5].

In a quantum weak measurement, there are three stages generally involved: First, a measured system is preselected in the initial state $|\psi_i\rangle$; then, a weak coupling between the observable $\hat{A}$ and the probe state is introduced; finally, the system is postselected as a final state $|\psi_f\rangle$. Here, the weak value is defined as

$$A_w = \frac{\langle \psi_f | \hat{A} | \psi_i \rangle}{\langle \psi_f | \psi_i \rangle}. \tag{1}$$

When the initial state and the final state are nearly orthogonal, the weak value can become quite large, leading to an amplification effect [6]. Therefore, weak measurements have been developed as precise metrology to amplify tiny physical effects, such as photonic spin Hall effect [7], ultrasmall phase shift [8,9], beam deflection [10], sub-Hertz resonance [11], single-photon polarization [12], and single-photon nonlinearity [13]. In addition, the weak measurement can also be used to observe Hardy's paradox [14,15] and average trajectories of single photons [16]. In standard quantum weak measurements [4,5], the preselection and the postselection of the quantum state are implemented in the same photon [Fig. 1(a)].

In this Letter, we address the question of whether the preselection and postselection can be performed in two different photons. We demonstrate this by utilizing polarization entanglement of pair photons we prepared [Fig. 1(b)]. The specially designed optical metasurface incorporating with the weak measurement system performs weak coupling and leads to a pointer shift. We then introduce the nonlocal weak measurement into the microscopy imaging system, and remotely achieve phase reconstruction of pure-phase objects. Most of the transparent biological specimens can be regarded as pure-phase objects, since they affect significantly only the phase of the input field [17]. Therefore, the nonlocal weak measurement provides possible applications in quantum microscope for label-free imaging of transparent biological cells and tissues.

Optical metasurfaces, as a class of optical metamaterials with a reduced dimensionality, have attracted much attention due to their fascinating abilities of controlling light [18–22]. Recently, metasurfaces have started making important progress in quantum photonics, where novel

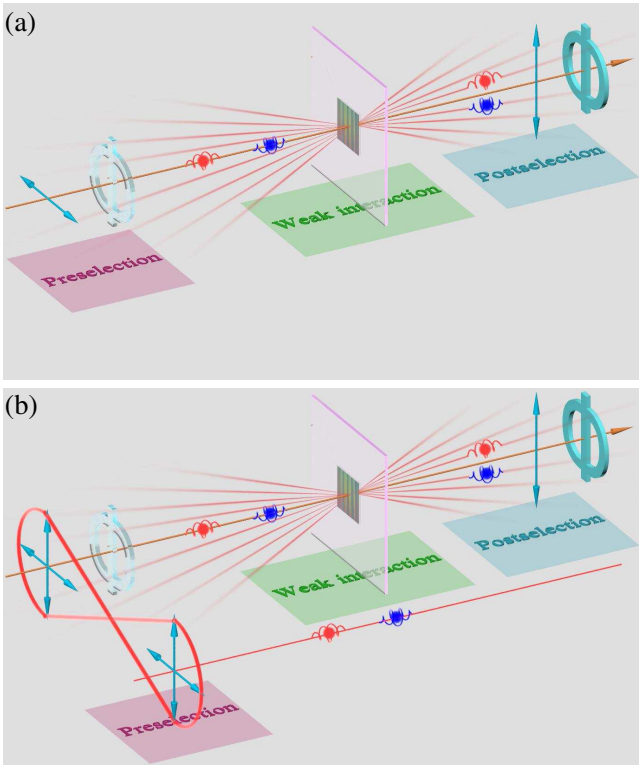

FIG. 1. Quantum weak measurements for phase reconstruction of pure-phase objects. (a) The scheme of standard weak measurements. Preselection and postselection of quantum state are implemented in the same photon. (b) The scheme of nonlocal weak measurements. Preselection and postselection are performed in two polarization entangled photons, respectively. The PB phase metasurface performs the weak coupling, and introduces a pointer shift.

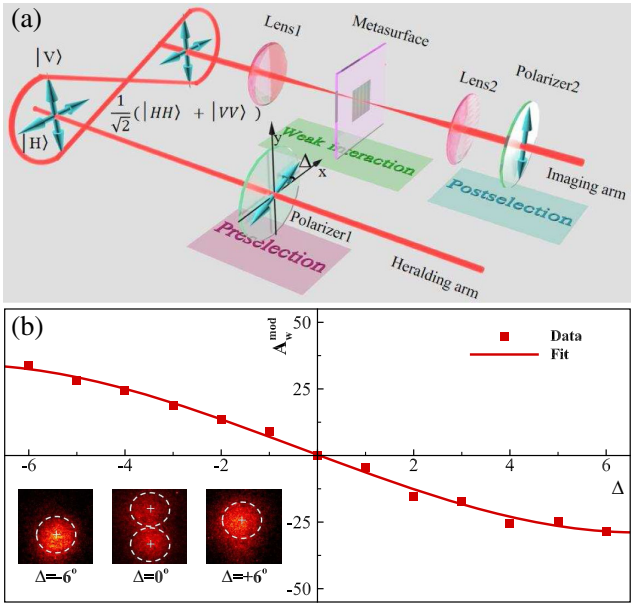

FIG. 2. Experimental measurement of entangled weak value by controlling the nonlocal preselection in the heralding arm. (a) Experimental scheme. In the imaging arm, a dielectric metasurface is placed on the focus plane of a $4f$ system to introduce a pointer shift, the polarizer 2 is used to implement the postselection. The polarization of entangled photon pairs is $(1/\sqrt{2})(|HH\rangle + |VV\rangle)$. The polarizer 1 in the heralding arm performs the preselection state with $|H - \Delta\rangle$. (b) The experimental results of the entangled weak value by adjusting the preselection in the heralding arm. The insets show the experimental images of intensity for different preselection states.

opportunities arose for the control of the nonclassical nature of light [23–32]. Here, the specially designed Pancharatnam-Berry (PB) phase metasurface is incorporated in a quantum weak measurement system to perform weak coupling between spin observable $\hat{\sigma}_3$ and the probe state. The metasurface is designed with homogeneous phase retardation π, and its optical axis direction periodically varies in the x direction with the period Λ. When a spin photon passes through the metasurface, the photon will acquire a space-variant PB phase $\Phi_{\mathrm{PB}} = 2\sigma_{\pm}\pi x/\Lambda$ [33,34]. The PB phase gradient leads to a momentum shift $\Delta k_x = \sigma_{\pm}\partial\Phi_{\mathrm{PB}}/\partial x$, where $\sigma_{\pm}$ correlates with two eigenvalues ± 1 of the spin photon. The photons will ultimately experience a real-space shift $\delta_i = (\Delta k_x/k_0)z$, which increases linearly with transmission distance z, where $k_0 = 2\pi/\lambda$. The real-space shift serves as the initial pointer shift to reveal the photon spin. The coupling strength can be precisely modulated by tailoring the unit structures of the PB phase metasurface.

In the standard weak measurement, the spin state of the observable [1], the strength of the coupling [7], and the wave function [2] can be measured precisely. Here, we want to realize the nonlocal reconstruction of the phase distribution of the wave function. There are two optical arms in the nonlocal weak measurement system: One is the imaging arm and the other is the heralding arm [Fig. 2(a)]. The preselection of the state in the heralding arm is chosen as $|H - \Delta\rangle$, while the postselection in the imaging arm as $|V\rangle$. In the spin basis, $|\psi_i\rangle = |H - \Delta\rangle = \exp(+i\Delta)|+\rangle + \exp(-i\Delta)|-\rangle$ and $|\psi_f\rangle = |V\rangle = i(|-\rangle - |+\rangle)$. Here, the preselection and postselection are implemented in two polarization entangled photons. In the spin basis, the observable $\hat{A}$ is set to be the Pauli operator $\hat{\sigma}_3$. Based on Eq. (1), the weak value can be obtained as $A_w = -i\cot\Delta$.

When the initial state and the final state are nearly orthogonal and $\langle\psi_f|\psi_i\rangle \to 0$, the weak value should be modified [see Supplemental Material, Sec. I [35]]. It shows that the pointer shift might be arbitrarily large when $\langle\psi_i|\psi_f\rangle \to 0$. In fact, the arbitrarily large pointer shift cannot be obtained. Thus, the weak value should be modified as $A_w^{\mathrm{mod}} = \delta_w/\delta_i$, and

$$A_w^{\mathrm{mod}} = -\frac{\sin 2\Delta}{\exp(2\delta_i^2/w^2) - \cos 2\Delta}. \tag{2}$$

Here, $\delta_w = \langle\phi_{\text{out}}|x|\phi_{\text{out}}\rangle/\langle\phi_{\text{out}}|\phi_{\text{out}}\rangle$ is the amplified pointer shift, w is the width of wave function. When the input wave function is a Gaussian distribution, the experimental result of modified weak value as a function of nonlocal preselection state is shown in Fig. 2(b). When the initial state and the final state faraway the orthogonal condition, $A_w^{\text{mod}} \simeq \text{Im}[A_w]$.

The phase distribution can be reconstructed precisely, if the weak value and pointer shift are determined. After the photon passes through the PB phase metasurface, the polarization evolves to a middle state:

$$|\psi_m\rangle = \exp(+i\Delta + ik_x\delta_i)|+\rangle + \exp(-i\Delta - ik_x\delta_i)|-\rangle. \quad (3)$$

Here, $\exp(i\hat{\sigma}_3 k_x\delta_i)$ denotes the spin-orbit coupling, and $|\hat{\sigma}_3 k_x\delta_i| \ll 1$ due to the fact that the spin-orbit coupling is a weak effect. After the preselection of state, weak coupling, and the postselection of state, the probe wave function in momentum space evolves to the final state:

$$|\tilde{\boldsymbol{\phi}}_{\text{out}}(k_x, k_y)\rangle = \langle\psi_f|\psi_i\rangle(1 + ik_x A_w\delta_i)|\tilde{\phi}_{\text{in}}(k_x, k_y)\rangle, \quad (4)$$

where $\tilde{\phi}_{\text{in}}(k_x, k_y)$ is the probe wave function in momentum space. Based on the Fourier transformation, the output wave function in real position space can be written as (see Supplemental Material, Sec. I [35])

$$|\phi_{\text{out}}(x, y)\rangle = \langle\psi_f|\psi_i\rangle\left(1 + A_w\delta_i\frac{\partial}{\partial x}\right)|\phi_{\text{in}}(x, y)\rangle. \quad (5)$$

Consider the probe wave function with pure-phase distribution $\phi_{\text{in}}(x, y) = \exp[i\varphi(x, y)]$, the intensity captured by the ICCD is proportional to the probability distribution $P(x, y) = \langle\phi_{\text{out}}|\phi_{\text{out}}\rangle$. If the preselected state and the postselected state is parallel ($\Delta = 90°$), the output can be seen as a bright-field image, which shows no contrast due to $P^{|V\rangle}(x, y) = |\exp[i\varphi(x, y)]|^2 = 1$. When the preselected state and the postselected state is orthogonal ($\Delta = 0°$), the output wave function can be written as the first-order spatial differentiation of input probe wave function: $|\phi_{\text{out}}(x, y)\rangle \propto \delta_i\partial|\phi_{\text{in}}(x, y)\rangle/\partial x$. The differential image can be obtained by $P^{|H\rangle}(x, y) = |\partial\phi_{\text{out}}(x, y)/\partial x|^2$. Here, the phase gradients can be converted into intensity-contrast image by the spatial differential operation. Therefore, the outline of phase objects can be observed clearly, since the phase gradient generally occurs at its edge [41,42].

When the preselected state is chosen as $|\psi_i\rangle = |H \pm \Delta\rangle$ and the postselected state $|\psi_f\rangle$ as $|V\rangle$, the relation between the phase gradient of the probe wave function and the probability distribution can be obtained as (see Supplemental Material, Sec. I [35])

$$P^{|H-\Delta\rangle}(x, y) - P^{|H+\Delta\rangle}(x, y) = -4|\langle\psi_f|\psi_i\rangle|^2\text{Im}[A_w]\delta_i\frac{\partial\varphi(x, y)}{\partial x}. \quad (6)$$

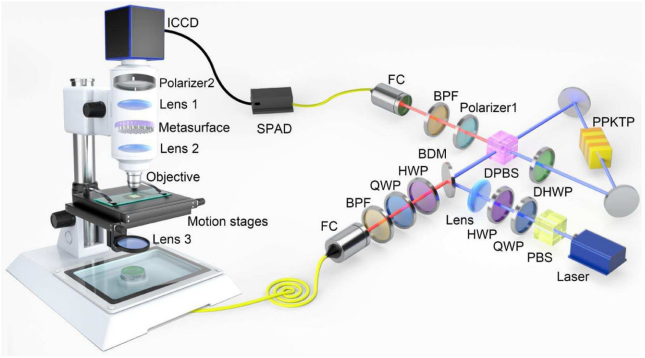

FIG. 3. Experimental setup of metasurface assisted quantum nonlocal weak-measurement microscope. Broadband dielectric mirror (BDM); periodically poled $KTiOPO_4$ crystal (PPKTP); dual-wavelength polarization beam splitter (DPBS); polarization beam splitter (PBS); dichromatic mirror (DM); fiber coupler (FC); band-pass filter (BPF); dual-wavelength half wave plate (DHWP); half wave plate (HWP); quarter wave plate (QWP); single photon avalanche detector (SPAD); intensified charge coupled device (ICCD). The blue (red) light path presents the 405 nm (810 nm) photons. The imaging system is composed of an objectives ($(10\times, \text{NA} = 0.25)$ and a $4f$ system. The PB phase metasurface performs a weak coupling and introduces a initial pointer shift. The preselection and the postselection are implemented by polarizer 1 and polarizer 2, respectively.

Therefore, the phase distribution can be reconstructed from measuring the output probability. Similarly, $\partial\varphi(x, y)/\partial y$ is also required for two-dimensional phase distributions. Finally, the phase distribution is reconstructed by 2D Fourier integration [43].

A schematic setup of the quantum nonlocal weak-measurement microscope is shown in Fig. 3. The microscope is consists of two parts: One is an imaging system; The other is a polarization entangled photon source. The integrated imaging system includes an objective, a PB phase metasurface, a $4f$ system, and a polarizer. Here, the PB phase metasurface provides the weak coupling and polarizer 2 performs the postselection of the polarized state. The polarization entangled photon source is composed of a pump laser and a Sagnac interferometer. A single-frequency diode laser at 405 nm is used as the pump source. Spontaneous parametric down-conversion happens when the pump light passes through a 20 mm long type-II phase matched PPKTP crystal. By adjusting the QWP and HWP in the pump beam, the pump power between clockwise and counterclockwise directions in Sagnac loop is kept balanced. A dual-wavelength polarization beam splitter (DPBS), two broadband dielectric mirrors and a dual-wavelength HWP (DHWP) are the components of the Sagnac interferometer. The DHWP is fixed at 45° to obtain the horizontal polarization of the counterclockwise pump directions in front of the crystal. The DPBS is used to separate the down-converted photon pairs pumped by two counterpropagating beams. By adjusting the combination

of HWP and QWP in the imaging arm, the output state of our quantum polarization entangled photon source turn out to be $|\Phi\rangle = (1/\sqrt{2})(|HH\rangle + |VV\rangle)$ [44,45].

Two-photon coincidence counts and polarization interference are performed to characterize the quality of the generated polarization entangled state. The imaging system is replaced by a SPAD in the coincidence counts. A polarizer is added in the imaging arm whose polarized axis is fixed at 0° or 45° to measure the polarization interference fringes [44]. The interference visibility is calculated as $V = (C_{\max} - C_{\min})/(C_{\max} + C_{\min})$, where $C_{\max}$ and $C_{\min}$ are maximum and minimum coincidence counts, respectively. Therefore, the visibilities of interference fringe are obtained as $96.4 \pm 0.1\%$ in the $+45°/-45°$ basis and $98.3 \pm 0.1\%$ in the H/V basis, respectively [35] (see Supplemental Material, Sec. II). The visibility bound required to violate the Bell's inequality is 71% [46,47]. Therefore, the polarization entangled photon source meets the requirement of nonlocal phase reconstruction.

The polarization entangled photons with the state of $(1/\sqrt{2})(|HH\rangle + |VV\rangle)$ are used as an illumination source to implement the phase reconstruction of pure-phase objects. When the state of input photons in heralding arm is set to $|H \pm \Delta\rangle$, thus the state of input photons in imaging arm will also be $|H \pm \Delta\rangle$. To demonstrate the nonlocal phase reconstruction from the phase gradient images using the quantum weak measurement microscope, two pure-phase objects etched with different letters are imaged. There are three steps to realize the nonlocal phase reconstruction of the phase distribution. First, we obtain the probability distribution $P^{|H+\Delta\rangle}(x, y)$ and $P^{|H-\Delta\rangle}(x, y)$ of the output image, which is achieved by remotely adjusting the preselection in the heralding arm with $|H + \Delta\rangle$ and $|H - \Delta\rangle$ ($\Delta = 3°$) [Figs. 4(a) and 4(d)]. It should be noted that the similar second-order correlation image with classical sources has been demonstrated [48]. Second, the differential images can be obtained by $|\partial\varphi(x, y)/\partial x + i\partial\varphi(x, y)/\partial y|$ [Figs. 4(b) and 4(e)]. Finally, the phase distributions are reconstructed as shown in Figs. 4(c) and 4(f). The reconstructed phase distribution shows high phase contrast, and the phase distribution of the phase objects is clearly observed.

We next demonstrate the nonlocal switch of three imaging modes that achieved by controlling the preselection in the heralding arm. The experimental results of bright-field, differential, and phase reconstruction imaging are shown in the Figs. 5(a)–5(c), respectively. When we adjust the preselected polarizer in the heralding arm to keep the input polarization state $|V\rangle$, the bright-field image is obtained, since the preselected state and postselected state is parallel [Fig. 5(a)]. In this case, the pure-phase object is invisible in the bright-field image. Then we make the polarization state of preselection as $|H\rangle$, and the differential imaging is achieved. The edge contour of the pure-phase object is revealed due to the differential operations, since

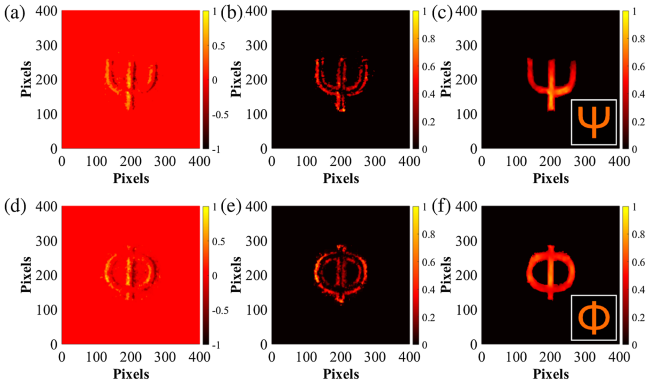

FIG. 4. Nonlocal phase reconstruction of transparent glass plate sample (model: BK7). Ψ and Φ shapes are etched on the glass surface with a 200 nm step using optical lithography. (a) and (d) The probability distribution $P^{|H-\Delta\rangle}(x, y) - P^{|H+\Delta\rangle}(x, y)$. (b) and (e) The deferential images of phase distribution $|\partial\varphi(x, y)/\partial x + i\partial\varphi(x, y)/\partial y|$. (c) and (f) The reconstructed phase distributions $\varphi(x, y)$. Insets in (c) and (f) show the designed phase distributions.

the phase gradient generally occurs at the edge [Fig. 5(b)]. However, it is still not enough to reveal the phase distribution. This problem can be solved by the reconstruction of phase distribution, which is achieved by adjusting the preselected state $|H \pm \Delta\rangle$. The phase distribution is reconstructed as shown in Fig. 5(c). The cross-section intensity distributions along the dashed lines in Figs. 5(a)–5(c) are shown in Figs. 5(d)–5(f), respectively.

In practical biological imaging applications, one can choose the desirable imaging mode to detect different characteristics of biological samples [49,50]. In the conventional microscopy imaging, the modulations of different imaging modes inevitably involve manual adjustment of optical elements in imaging system, such as polarizers and filters, resulting in possible misalignment of the optical

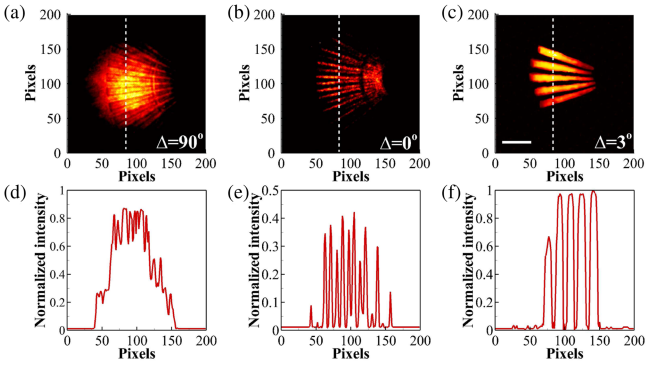

FIG. 5. Nonlocal switch of different imaging modes in the imaging arm based on the remote modulation of preselections in the heralding arm. (a) Bright-field image ($\Delta = 90°$). (b) Differential image ($\Delta = 0°$). (c) Phase reconstruction image ($\Delta = 3°$). (d)–(f) are taken along the white dashed lines in (a)–(c), respectively. Scale bar, 100 μm.

path. In our scheme, a pair of entangled photons are strong correlated, and one can influence the other instantaneously although they are far apart. Therefore, different imaging modes are nonlocally controlled by the preselection in the heralding arm, without changing anything on the imaging arm. This is impossible to be achieved by using a conventional microscope with classical sources.

In low photon regime, our nonlocal weak measurement scheme has a higher image contrast than the standard one. Here, the image contrast is defined as $C = (I_{\max} - I_{\min})/(I_{\max} + I_{\min})$, where $I_{\max}$ and $I_{\min}$ are maximum and minimum intensity, respectively [51]. In the standard weak-measurement imaging scheme, the ICCD is internally triggered. Both the signal photons and environmental noise photons will be continuously accumulated during the imaging process. Therefore, a low image contrast ($C \approx 0.27$) is inevitable when the signal photon level is comparable to environmental photon noise. The effects of environmental noise can be effectively reduced by increasing the intensity of the illumination light. For photosensitive biological samples, however, the biophysical damage typically arises due to the large illumination intensities. In the nonlocal weak-measurement imaging scheme, the ICCD is externally triggered, and the signal photons are accumulated in the ICCD only within a short time window (4 ns). Almost all noise photons are prevented from detection, and therefore achieve a higher image contrast and signal-to-noise of image (see Supplemental Material, Sec. IV [35]). Here, we obtain a phase reconstruction image of the pure-phase test target with a high contrast of $C \approx 0.95$ (see Supplemental Material, Sec. III [35]).

In conclusion, we have proposed and demonstrated a quantum microscopy based on metasurface-assisted nonlocal weak measurement. In our weak measurement scheme, the preselection and postselection of the quantum state are implemented by a polarization entangled photon pair, and the weak coupling is performed by Pancharatnam-Berry phase metasurface. By introducing the nonlocal weak measurement into microscopy imaging system, it allows us to remotely reconstruct the phase distribution of transparent samples. Different microscopy imaging modes, including bright-field, differential, and phase reconstruction, can be achieved by remotely controlling the preselection in the heralding arm. We have shown that the nonlocal weak measurement can outperform standard weak measurements in phase construction at the very low photon level. The quantum microscope is an important tool to characterize the biological samples and understand the dynamics of a living system with quantum illumination [52–56]. We believe that our result paves a possible way towards the quantum weak-measurement microscope for label-free imaging of transparent biological cells and tissues.

This work was supported by the National Natural Science Foundation of China (Grants No. 12174097 and No. 61835004), Natural Science Foundation of Hunan Province (Grant No. 2021JJ10008), and Postdoctoral Science Foundation of China (Grants No. BX20230116 and No. 2023M741135).

*hailuluo@hnu.edu.cn

[1] Y. Aharonov, D. Z. Albert, and L. Vaidman, How the result of a measurement of a component of the spin of a spin-$\frac{1}{2}$ particle can turn out to be 100, Phys. Rev. Lett. **60**, 1351 (1988).
[2] J. S. Lundeen, B. Sutherland, A. Patel, C. Stewart, and C. Bamber, Direct measurement of the quantum wavefunction, Nature (London) **474**, 188 (2011).
[3] J. Z. Salvail, M. Agnew, A. S. Johnson, E. Bolduc, J. Leach, and R. W. Boyd, Full characterization of polarization states of light via direct measurement, Nat. Photonics **7**, 316 (2013).
[4] A. G. Kofman, S. Ashhab, and F. Nori, Nonperturbative theory of weak pre- and postselected measurements, Phys. Rep. **520**, 43 (2012).
[5] J. Dressel, M. Malik, F. M. Miatto, A. N. Jordan, and R. W Boyd, Colloquium: Understanding quantum weak values: Basics and applications, Rev. Mod. Phys. **86**, 307 (2014).
[6] A. N. Jordan, J. Martínez-Rincón, and J. C. Howell, Technical advantages for weak-value amplification: When less is more, Phys. Rev. X **4**, 011031 (2014).
[7] O. Hosten and P. Kwiat, Observation of the spin Hall effect of light via weak measurements, Science **319**, 787 (2008).
[8] N. Brunner and C. Simon, Measuring small longitudinal phase shifts: Weak measurements or standard interferometry?, Phys. Rev. Lett. **105**, 010405 (2010).
[9] X.-Y. Xu, Y. Kedem, K. Sun, L. Vaidman, C.-F. Li, and G.-C. Guo, Phase estimation with weak measurement using a white light source, Phys. Rev. Lett. **111**, 033604 (2013).
[10] P. B. Dixon, D. J. Starling, A. N. Jordan, and J. C. Howell, Ultrasensitive beam deflection measurement via interferometric weak value amplification, Phys. Rev. Lett. **102**, 173601 (2009).
[11] W. Qu, S. Jin, J. Sun, L. Jiang, J. Wen, and Y. Xiao, Sub-Hertz resonance by weak measurement, Nat. Commun. **11**, 1752 (2020).
[12] G. J. Pryde, J. L. OBrien, A. G. White, T. C. Ralph, and H. M. Wiseman, Measurement of quantum weak values of photon polarization, Phys. Rev. Lett. **94**, 220405 (2005).
[13] A. Feizpour, X. Xing, and A. M. Steinberg, Amplifying single-photon nonlinearity using weak measurements, Phys. Rev. Lett. **107**, 133603 (2011).
[14] J. S. Lundeen and A. M. Steinberg, Experimental joint weak measurement on a photon pair as a probe of hardys paradox, Phys. Rev. Lett. **102**, 020404 (2009).
[15] K. Yokota, T. Yamamoto, M. Koashi, and N. Imoto, Direct observation of Hardys paradox by joint weak measurement with an entangled photon pair, New J. Phys. **11**, 033011 (2009).
[16] S. Kocsis, B. Braverman, S. Ravets, M. J. Stevens, R. P. Mirin, L. K. Shalm, and A. M. Steinberg, Observing the average trajectories of single photons in a two-slit interferometer, Science **332**, 1170 (2011).

[17] Y. Park, C. Depeursinge, and G. Popescu, Quantitative phase imaging in biomedicine, Nat. Photonics **12**, 578 (2018).
[18] N. Yu, P. Genevet, M. A. Kats, F. Aieta, Jean-Philippe Tetienne, F. Capasso, and Z. Gaburro, Light propagation with phase discontinuities: Generalized laws of reflection and refraction, Science **334**, 333 (2011).
[19] X. Yin, Z. Ye, J. Rho, Y. Wang, and X. Zhang, Photonic spin Hall effect at metasurfaces, Science **339**, 1405 (2013).
[20] A. V. Kildishev, A. Boltasseva, and V. M. Shalaev, Planar photonics with metasurfaces, Science **339**, 1232009 (2013).
[21] D. Lin, P. Fan, E. Hasman, and M. L. Brongersma, Dielectric gradient metasurface optical elements, Science **345**, 298 (2014).
[22] B. Xiong, Y. Liu, Y. Xu, L. Deng, C.-W. Chen, J.-N. Wang, R. Peng, Y. Lai, Y. Liu, and M. Wang, Breaking the limitation of polarization multiplexing in optical metasurfaces with engineered noise, Science **379**, 294 (2023).
[23] P. K. Jha, X. Ni, C. Wu, Y. Wang, and X. Zhang, Metasurface-enabled remote quantum interference, Phys. Rev. Lett. **115**, 025501 (2015).
[24] T. Stav, A. Faerman, E. Maguid, D. Oren, V. Kleiner, E. Hasman, and M. Segev, Quantum entanglement of the spin and orbital angular momentum of photons using metamaterials, Science **361**, 1101 (2018).
[25] K. Wang, J. G. Titchener, S. S. Kruk, L. Xu, H.-P. Chung, M. Parry, I. I. Kravchenko, Y.-H. Chen, A. S. Solntsev, Y. S. Kivshar, D. N. Neshev, and A. A. Sukhorukov, Quantum metasurface for multiphoton interference and state reconstruction, Science **361**, 1104 (2018).
[26] L. Li, Z. Liu, X. Ren, S. Wang, V.-C. Su, M.-K. Chen, C. H. Chu, H. Y. Kuo, B. Liu, W. Zang, G. Guo, L. Zhang, Z. Wang, S. Zhu, and D. P. Tsai, Metalens-array-based high-dimensional and multiphoton quantum source, Science **368**, 1487 (2020).
[27] J. Zhou, S. Liu, H. Qian, Y. Li, H. Luo, S. Wen, Z. Zhou, G. Guo, B. Shi, and Z. Liu, Metasurface enabled quantum edge detection, Sci. Adv. **6**, eabc4385 (2020).
[28] Q. Li, W. Bao, Z. Nie, Y. Xia, Y. Xue, Y. Wang, S. Yang, and X. Zhang, A non-unitary metasurface enables continuous control of quantum photon-photon interactions from bosonic to fermionic, Nat. Photonics **15**, 267 (2021).
[29] A. S. Sointsev, G. S. Agarwal, and Y. Kivshar, Metasurfaces for quantum photonics, Nat. Photonics **15**, 327 (2021).
[30] W. J. M. Kort-Kamp, A. K. Azad, and D. A. R. Dalvit, Space-time quantum metasurfaces, Phys. Rev. Lett. **127**, 043603 (2021).
[31] T. Santiago-Cruz, S. D. Gennaro, O. Mitrofanov, S. Addamane, J. Reno, I. Brener, and M. V. Chekhova, Resonant metasurfaces for generating complex quantum states, Science **377**, 991 (2022).
[32] Y. Gao, Z. Wang, Y. Jiang, R. Peng, Z. Wang, D. Qi, R. Fan, W. Tang, and M. Wang, Multichannel distribution and transformation of entangled photons with dielectric metasurfaces, Phys. Rev. Lett. **129**, 023601 (2022).
[33] X. Ling, X. Zhou, Y. Yi, W. Shu, Y. Liu, S. Chen, H. Luo, S. Wen, and D. Fan, Giant photonic spin Hall effect in momentum space in a structured metamaterial with spatially varying birefringence, Light Sci. Appl. **4**, e290 (2015).
[34] J. Zhou, H. Qian, C.-F. Chen, J. Zhao, G. Li, Q. Wu, H. Luo, S. Wen, and Z. Liu, Optical edge detection based on high efficiency dielectric metasurface, Proc. Natl. Acad. Sci. U.S.A. **116**, 11137 (2019).
[35] See Supplemental Material at http://link.aps.org/supplemental/10.1103/PhysRevLett.132.043601 for information about derivation of the phase distribution reconstruction, two-photon coincidence counts, image contrast enhance in nonlocal weak measurement, and signal-to-noise ratio of pointer shift and phase image, which includes Refs. [36–40].
[36] S. M. Barnett, C. Fabre, and A. Maître, Ultimate quantum limits for resolution of beam displacements, Eur. Phys. J. D **22**, 513 (2003).
[37] D. J. Starling, P. B. Dixon, A. N. Jordan, and J. C. Howell, Optimizing the signal-to-noise ratio of a beam-deflection measurement with interferometric weak values, Phys. Rev. A **80**, 041803(R) (2009).
[38] S. Johnson, A. McMillan, C. Torre, S. Frick, J. Parity, and M. Padgett, Single-pixel imaging with heralded single photons, Opt. Continuum. **1**, 826 (2022).
[39] J. A. Kahana, B. J. Schnapp, and P. A. Silver, Kinetics of spindle pole body separation in budding yeast, Proc. Natl. Acad. Sci. U.S.A. **92**, 9707 (1995).
[40] B. Rappaz, E. Cano, T. Colomb, J. Kuhn, C. Depeursinge, V. Simanis, P. J. Magistretti, and P. Marque, Noninvasive characterization of the fission yeast cell cycle by monitoring dry mass with digital holographic microscopy, J. Biomed. Opt. **14**, 034045 (2009).
[41] J. Zhou, H. Qian, J. Zhao, M. Tang, Q. Wu, M. Lei, H. Luo, S. Wen, and Z. Liu, Two-dimensional optical spatial differentiation and high-contrast imaging, Natl. Sci. Rev. **8**, nwaa176 (2021).
[42] J. Liu, Q. Yang, S. Chen, Z. Xiao, S. Wen, and H. Luo, Intrinsic optical spatial differentiation enabled quantum dark-field microscopy, Phys. Rev. Lett. **128**, 193601 (2022).
[43] R. Wang, S. He, and H. Luo, Photonic spin-Hall differential microscopy, Phys. Rev. Appl. **18**, 044016 (2022).
[44] T. Kim, M. Fiorentino, and F. N. C. Wong, Phase-stable source of polarization-entangled photons using a polarization Sagnac interferometer, Phys. Rev. A **73**, 012316 (2006).
[45] B. Fickler, M. Krenn, R. Lapkiewicz, S. Ramelow, and A. Zeilinger, Real-time imaging of quantum entanglement, Sci. Rep. **3**, 1914 (2013).
[46] J. F. Clauser and A. Shimony, Bell's theorem: Experimental tests and implications, Rep. Prog. Phys. **41**, 1881 (1978).
[47] R. Horodecki, P. Horodecki, M. Horodecki, and K. Horodecki, Quantum entanglement, Rev. Mod. Phys. **81**, 865 (2009).
[48] J. Wen, Forming positive-negative images using conditioned partial measurements from reference arm in ghost imaging, J. Opt. Soc. Am. A **29**, 1906 (2012).
[49] F. Zernike, How I discovered phase contrast, Science **121**, 345 (1955).
[50] R. Allen, G. David, and G. Nomarski, The Zeiss-Nomarski differential interference equipment for transmitted-light

microscopy, Z. Wiss. Mikrosk. Mikrosk. Tech. **69**, 193 (1969).

[51] P. A. Morris, R. S. Aspden, J. E. C. Bell, R. W. Boyd, and M. J. Padgett, Imaging with a small number of photons, Nat. Commun. **6**, 5913 (2015).

[52] T. Ono, R. Okamoto, and S. Takeuchi, An entanglementenhanced microscope, Nat. Commun. **4**, 2426 (2013).

[53] Y. Israel, S. Rosen, and Y. Silberberg, Supersensitive polarization microscopy using NOON states of light, Phys. Rev. Lett. **112**, 103604 (2014).

[54] D. G. England, B. Balaji, and B. J. Sussman, Quantum enhanced standoff detection using correlated photon pairs, Phys. Rev. A **99**, 023828 (2019).

[55] R. Tenne, U. Rossman, B. Rephael, Y. Israel, A. Krupinski-Ptaszek, R. Lapkiewicz, Y. Silberberg, and D. Oron, Super-resolution enhancement by quantum image scanning microscopy, Nat. Photonics **13**, 116 (2019).

[56] C. A. Casacio, L. S. Madsen, A. Terrasson, M. Waleed, K. Barnscheidt, B. Hage, M. A. Taylor, and W. P. Bowen, Quantum-enhanced nonlinear microscopy, Nature (London) **594**, 201 (2021).